Preprint Title	Ultra-low energy amorphization of contaminated silicon samples investigated by Molecular Dynamics
Authors	Grégoire R. N. Defoort-Levkov, Alan S. Bahm and Patrick Philipp
Publication Date	24 März 2023
Article Type	Full Research Paper
Supporting Information File 1	Ar_Si_Energy_Variation_Supporting_Information_v2.docx; 1.5 MB
ORCID® iDs	Grégoire R. N. Defoort-Levkov - https://orcid.org/0000-0001-8514-3817; Patrick Philipp - https://orcid.org/0000-0001-5219-5178

Ultra-low energy amorphization of contaminated silicon samples investigated by Molecular Dynamics

Grégoire R.N. Defoort-Levkov*[1,2], Alan Bahm [3], Patrick Philipp *[1]

1 – Advanced Instrumentation for Nano-Analytics (AINA), Materials Research and Technology Department (MRT), Luxembourg Institute of Science and Technology (LIST), 4422 Belvaux, Luxembourg.

2 – University of Luxembourg, 4365 Esch-sur-Alzette, Luxembourg.

3 – Thermo Fisher Scientific, Hillsboro, OR, 97124, USA

Email: Patrick Philipp – patrick.philipp@list.lu

* Corresponding author

The manuscript was written through contributions of all authors. All authors have given approval to the final version of the manuscript.

Abstract

Ion beam processes related to focused ion beam (FIB) milling, surface patterning and secondary ion mass spectrometry (SIMS) require precision and control, the quality and cleanliness of the sample being a detrimental factor. Furthermore, several domains of nanotechnology and industry use nano-scaled samples that need to be controlled to an extreme level of precision. To reduce the irradiation-induced damage and to limit the interactions of the ions with the sample, low energy ion beams are used due to their low implantation depths. Yet, low energy ion beams come with a variety of challenges. Indeed, for such low energies, the residual gas molecules in the instrument chamber can adsorb on the sample surface and impact the ion beam processes. In this paper we pursue an investigation on the effects of the most common contaminant, water, sputtered by ultra-low energy ion beams, ranging from 50 to 500 eV and covering the full range of incidence angles, using Molecular Dynamics (MD) simulations with the ReaxFF potential. From this study we show that the expected sputtering yields trends are respected down to the lowest sputtering yields, a region of interest with low damage being obtained for incidence angles around 60 to 75°. We also demonstrate that higher energies induce a larger removal of the water contaminant and at the same time induce an increased amorphization, which produces a trade-off between sample cleanliness and damage.

Keywords

Molecular dynamics, Simulations, Silicon, Contamination, Water, Argon, ion bombardment, Angle dependency, Energy dependency, Low energy

Introduction

Low energy ion beams present substantial improvements and possibilities to reduce the damage production on the surface of samples[1,2]. In the recent years, the need to control what happens at the surface of the sample has risen sharply, specifically for semiconductors[3,4], microelectronics[5] and surface patterning[6,7]. Other applications of low energy beams include the preparation of nanoholes[8,9]. Furthermore, deposition processes are substantially more controllable at a low energy[10,11], which also makes such beams a valid candidate for these processes.

Another application includes lamella preparation for transmission electron microscopy (TEM). TEM and scanning electron microscopy (SEM) have high constraints of cleanliness[12]. TEM samples require a small thickness[13] and are usually prepared thanks to ion milling processes[14,15], which rely heavily on the precise ablation of materials to preserve the crystalline structure of the analyzed sample. These samples, usually shaped as lamellas, are very sensitive to contaminations[16] and environment changes during their preparation to the point where, if exposed to contamination, the oxide layer formed on the surface of the lamella could complicate analysis[17,18]. While this oxide layer has a substantial impact, ion induced damage contributes even more to the degradation of the sample[19], due to an in-depth amorphization.

Here, a low energy ion beam (i.e. impact energies below 1 keV) could offer increased precision during the milling process[20] as well as substantially reduced damage near the surface of the samples, de-facto preserving the structure of the sample as closely as possible, which includes the minimization of the thickness of the amorphous layer. Focused ion beams of such low energy are generally hard to achieve due to the difficulty of focusing. . With this setup it is possible to reach ion beams down to 50 eV. Some instruments now-a-days can utilize focused beams of 500 eV to perform chemical analysis of material[21], and it is planned to reach down to 50 eV in a near future, which would be correspondingly surface sensitive.

In both previously mentioned cases, contaminations in the experimental chamber play an important role for the sputtering processes. Typical contaminations are (by order of frequency): water, nitrogen, carbon and carbonated components that can be found in the atmosphere[22–24], residuals coming from past experiments in the chamber, which can include silicon, carbon, or any type of particles that would have been sputtered previously and adsorbed on the walls of the sample chamber[24,25]. The work in this paper, will be based on methodologies developed in a previous paper[26], which focused on a silicon sample contaminated with a water layer and in which we showed the influence of the contamination layer on the sputtering process. With the presence of water on the sample surface, we showed that while the amorphization depth was substantially increased, the silicon sputtering yield was not impacted significantly. In this article, we will use the incidence angles of 0, 30, 45, 60, 75 and 83°, defined with respect to the surface normal, and the ultra-low impact energies of 50, 100, 200, 300, 400 and 500 eV. Our aim is to determine the optimal conditions to reduce the damage formation near the surface, while also retaining a high degree of contaminant removal. All the bombardments have been simulated using a Reactive Force Field (ReaxFF)[27,28] and the Molecular Dynamics (MD) code LAMMPS[29]. IWhile low energy ion beams are hard to achieve experimentally, in simulations such beams are easy to model. In this paper, by studying the differences between the higher (500 eV) and the lower (50 eV) impact energies, we will show the differences in the amorphization processes. While higher energies increase amorphization, as expected, we will also show that the favorable angle to minimize the implantation of the species of the contamination layer is in the 60 to 75° angles range.

Computational methods

Force fields

The force fields used to simulate the ion bombardment of a contaminated silicon sample have already been described in a previous article [37]. To summarize, it is composed of a set of two potentials:

- The Reactive Force Field (ReaxFF)[28] designed to compute the bonds between silicon, oxygen and hydrogen atoms, as well as the computing of the distribution of partial charges to model the bond formation and breaking in the sample.
- The Morse potential[30] is used to model the interactions of the argon particles with the other species. Since argon atoms are inert and are only interacting very

weakly with the sample atoms, a simple Morse potential is enough to describe these interactions.

ReaxFF potentials are derived from quantum mechanics calculations[31,32] and allow to model the bond formation and breaking with good precision and reasonable computation costs. For our simulations, this information is of critical importance since it allows us to describe precisely the interactions taking place during the ion bombardment near the sample surface. Oxygen and silicon have a particularly strong interaction[33,34] and partial charges contribute significantly to the bond energy. ReaxFF potentials can describe this phenomenon and, allow to simulate the response of the sample while bombarded with different conditions (e.g. different energies and angles). The ReaxFF potential uses the QEq charge equilibration method[31,35,36] which is important because this method provides the partial charges for various chemical environments.

On the other hand, the simplicity of the Morse potential allowed us to represent the interactions between the full valence band argons atoms and the sample atoms. As described in previous work[26], a set of DFT calculations were performed using VASP to compute the Morse potential for argon – silicon, argon – hydrogen and argon – oxygen interactions.

Molecular dynamics setup

The simulation system is made of a box periodic in X and Y dimensions, and aperiodic in Z the dimension. It contains a sample of 5248 atoms (silicon, and a thin layer of water molecules). The simulations are performed using the LAMMPS molecular dynamics code on the HPC cluster of the Luxembourg Institute of Science and Technology. The simulations aim to reproduce a continuous sputtering process in experiments: argon atoms are accelerated (at various angles and energies) towards the sample surface, the resulting collision cascade is modelled in the sample containing all the atoms, exported, and re-used for following ion impacts. By increasing the number of ion impacts, a higher fluence is reached, e.g 500 ion bombardments on a surface of 18.9 nm² results in a fluence of 2.6 x 10^{15} atoms/cm². A more in-depth description of the full preparation of the sample and the workflow for continuous ion bombardment is given in a previous publication[26].

In the current study we will focus on the impact of energy variations on the sputtering processes, while discussing the angle dependency for some conditions. To perform such analysis, we selected several angles and energy:

- For the impact energy, we selected 50, 100, 200, 300, 400 and 500 eV to stay in the ultra-low energy domain.
- For the angles we selected 0, 30, 45, 60, 75 and 83° with respect to the surface normal since they cover the full range. We will specifically elaborate the discussion around the grazing incidence angles which are of interest for the applications of the ultra-low energy ion beams.

The innovative part of the simulation process comes from the presence of a contamination layer on top of the sample, as well as the continuous sputtering process which can be decomposed in two steps: a bombardment step where the argon ions are shot at an angle and at a specific energy towards the sample, and a cool-down step where the target is cooled down until it reaches room temperature again. All the simulations are done at 300 K to reproduce ion beam processes at room temperature.

Results and discussion

In figure **1** the status of the sample after 500 impacts (corresponding to a fluence of 2.6 x 10^{15} at.cm^{-2}) is represented for each impact energy investigated in this study and for an incidence angle of 45° with respect to the surface normal. We selected 45° for this representation as it is a good angle for the observation of a significant number of Ar implantations (maximal at normal incidence) and for some significant amorphization (maximal at angles close to 60 – 75°). Higher impact energies will induce deeper damage as well as increased sputtering yields, hence the depth of the crater will increase with impact energy.

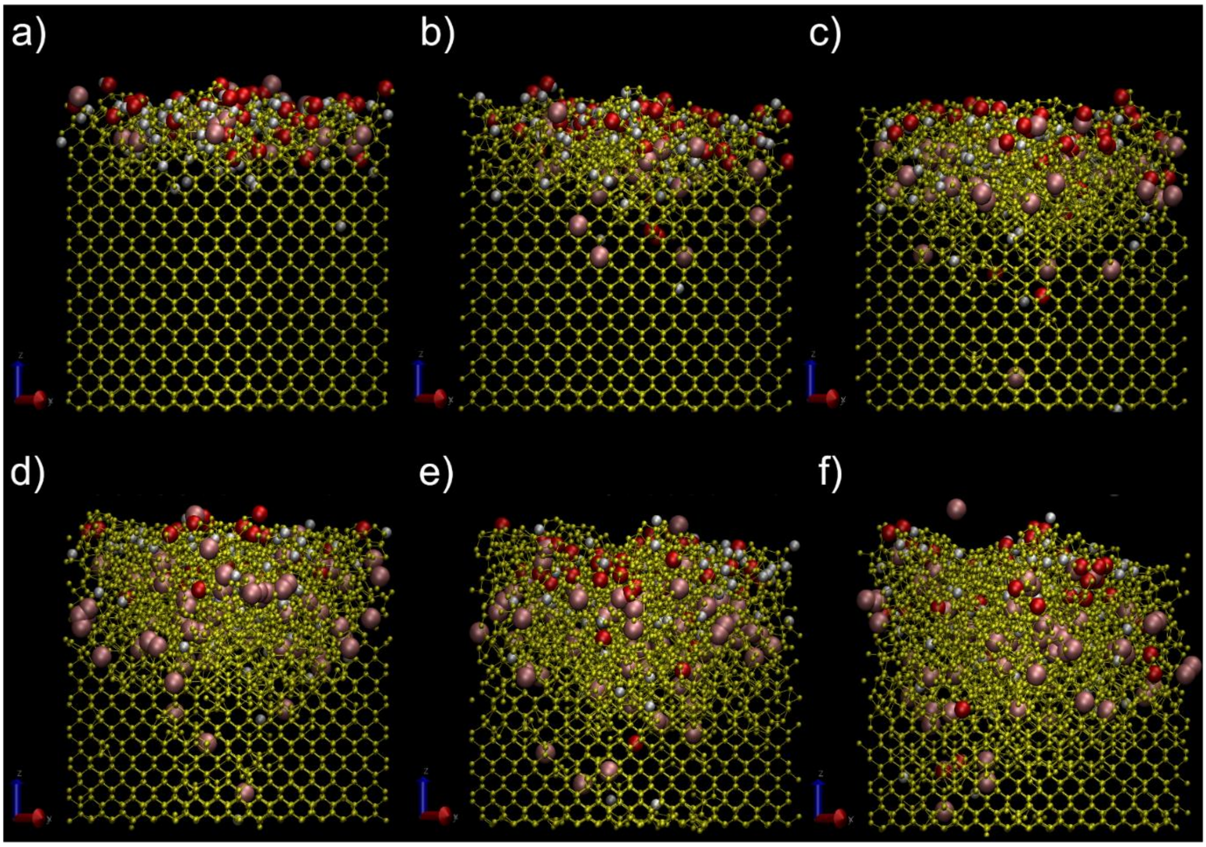

Figure 1: Representations of the contaminated sample under argon irradiation for an incidence angle of 45° and for a) 50 eV, b) 100 eV, c) 200 eV, d) 300 eV, e) 400 eV and f) 500 eV. The sample is oriented in the (110) direction.

The methodology to characterize irradiation-induced sample modifications and sputtering processes are like the ones used in the previous study. In this publication, the focus is on impact energy variations. We should expect significant variations in sputtering yields, damage formation and amount of material displaced. We will also study the fragmentation, implantation and sputtering of water molecules, which is another interesting aspect of the analysis methodology.

Amorphization coefficient variation

The amorphization coefficient used to characterize damage formation in the irradiated sample is a modification of the strain formula adjusted to the needs of the MD simulations in this work and is described in the equation (1):

$$\mu = \frac{1}{n_{Bonds}} \sum_{n_{Bonds}} \left[1 - \left| \frac{BondLength_{Theory} - BondLength_{Measured}}{BondLength_{Theory}} \right| \right] \quad (1)$$

The samples are divided into slabs of an equal thickness of one lattice height. According to the value of the amorphization coefficient calculated in each slab, we could identify three regions of interest:

- the crystalline region, which corresponds to values of the amorphization coefficient $\mu > 0.94$ and indicates a pristine crystalline structure. This region is situated closer to the bottom of the sample.
- The amorphous region, where $\mu < 0.89$ and no local order is present. It is located near the surface.
- A transitive region that we label “partially amorphous region” and where $0.89 < \mu < 0.94$. The damage induced by ion irradiation has not yet completely disturbed the local order. It is always located between the crystalline and amorphous slabs.

In the crystalline region the sample is intact and only thermal vibrations occurs. The amorphous region has been damaged by the recoil atoms and argon ions and the crystalline structure is not present anymore. The transitive region is a buffer region in which some damage can be found but the crystalline structure is preserved to some degree. This buffer is most of the time 1 unit cell thick but can yield higher values in some cases that will be discussed later. For instance, at normal incidence the damage is localized but penetrates deeply, inducing a thicker buffer between the crystalline region and the amorphous region.

In **figure 2,** the variations of the amorphization coefficient are plotted for several angles with respect to the impact energy. For all energies, the thickness of the amorphous region is smaller for higher incidence angles. This can prove especially useful since 500 eV argon beams can be collimated more easily than 50 eV beams, yet no significant modification of the amorphous layer thickness is observed. To complement the observations on the amorphous layer thickness, we will study in later sections several other parameters to corroborate this hypothesis. Moreover, for 83°, the sample keeps a pristine layer whereas for almost all other angles, at higher impact energies, the sample is damaged to the point where almost no crystalline structure remains (see supplementary information).. Supplementary material shows the variation of the amorphization coefficient, taking for basis 50 and 500 eV collisions, and in which we display all the angles, allowing a good comparison for the damage done at higher angles. In this configuration, the partially amorphous slab has an increased in thickness due to the implantation of the higher energy argon ions.

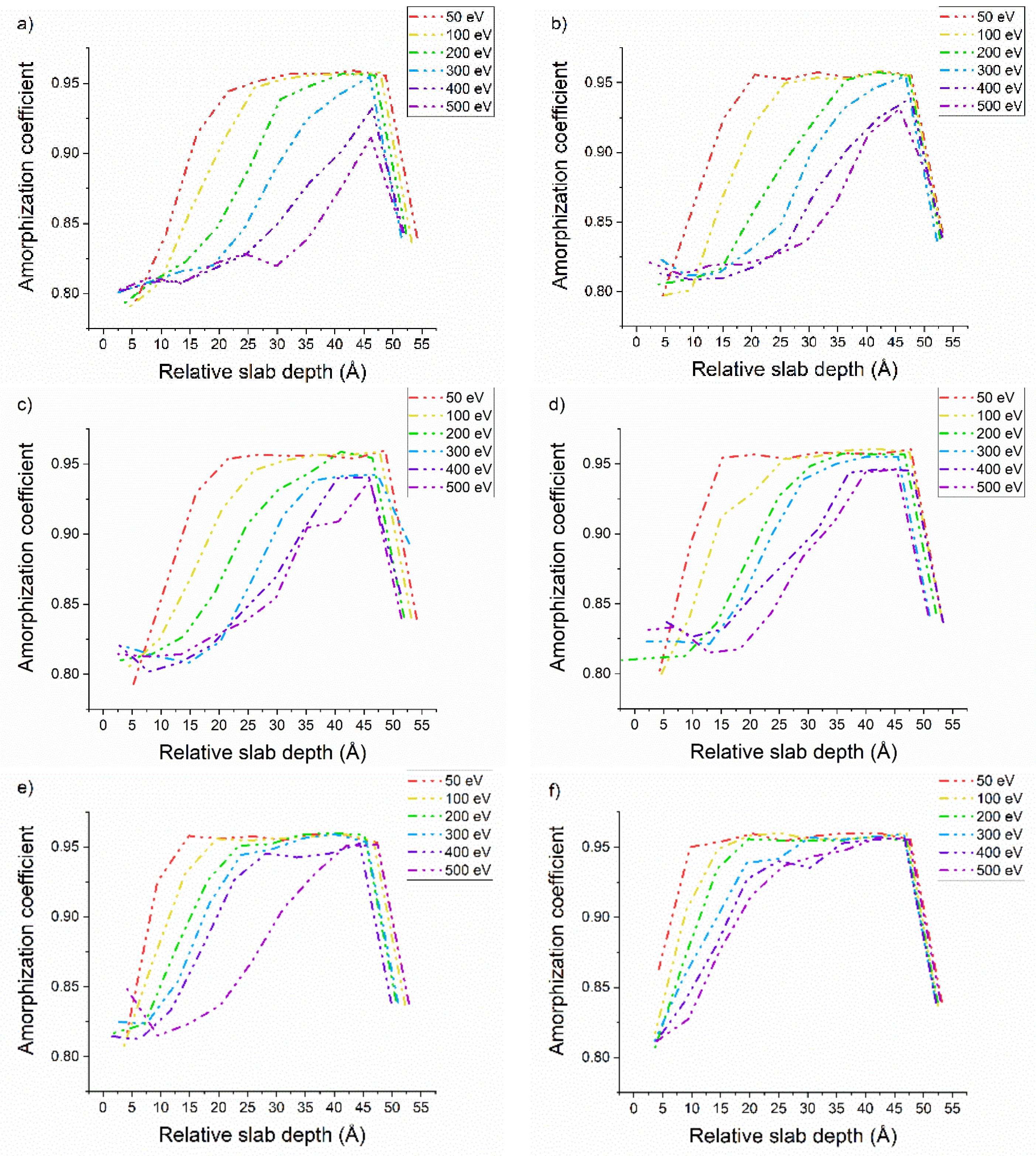

Figure 2: Evolution of the amorphization coefficient with respect to energy for a) 0°, b) 30°, c) 45°, d) 60°, e) 75° and f) 83°. The low values at a depth around 53 Å are due to the dimers formed at the bottom surface of the sample during the equilibration process.

To elaborate the analysis of the amorphization coefficient, we plotted the variation of the thickness for each region of interest for all the simulation conditions. In **figure 3** we observe the evolution of the slab's thickness for the amorphous and partially amorphous regions. The thickness of the crystalline slab is always the difference between the total sample thickness and the thickness of the amorphous and partially amorphous slabs, we included it in the supporting information. The thickness of the amorphous slab, regardless of the angle, evolves almost linearly with respect to the impact energy. The thickness of the amorphous slab is the same at 83 degrees 500 eV and 45 degrees 200 eV. This supports the idea that grazing angle collisions deliver less damage. The thickness of the partially amorphized region varies due to changes in beam energy and incidence angle.T. and is related to the extend of the collision cascade. This behavior induces localized concentration of damage which can, at certain angles channel deeper in the bulk, causing some extremely localized disorder that would disturb enough the lattice to modify the amorphous coefficient value below the threshold for the crystalline characterization. An extensive characteristic that can be studied easily in each of our slabs is the radial distribution function, as it allows to confirm the nature of each slab by studying the local order / disorder.

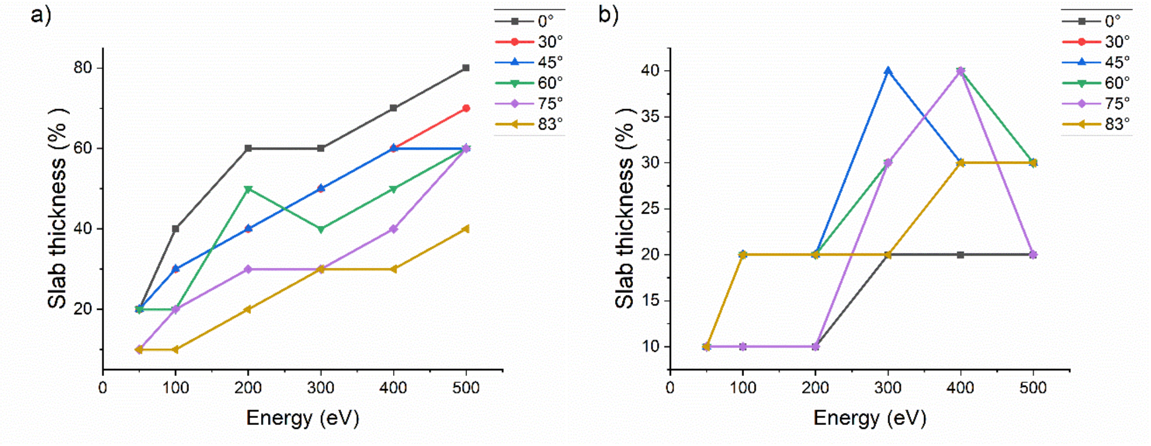

Figure 4: Evolution of the thickness of a) the amorphous region and b) the partially amorphous region for each energy with respect to the angle.

Radial distribution function

The radial distribution function (RDF) allows to study the variations in crystalline structure in the sample by quantitatively characterizing the number of atomic neighbors. The RDF acts as a good estimator of the local order (or disorder) of the sampleand complements the amorphization coefficient. The RDF was computed by the algorithm provided by Kopera et al. [37] . In **figure 5** we can observe the variations of the RDF with respect to the energy for 30° and 75° argon ion collisions, for each of the 3 regions (crystalline, partially amorphous and completely amorphous).

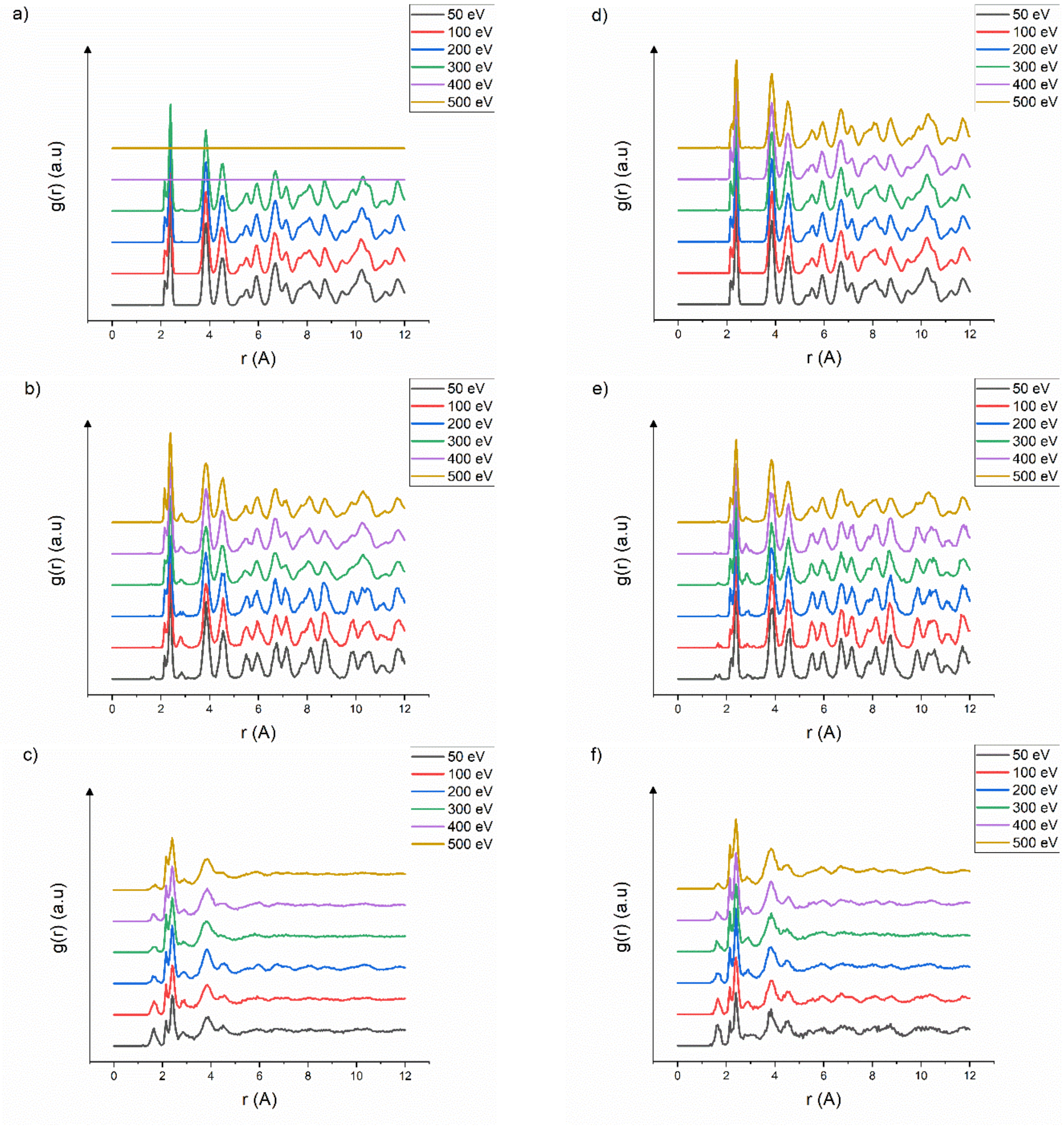

Figure 5: Evolution of the RDF for each slab, at 30° and 75° collisions. In order from crystalline to amorphous for a –c) 30° and d – f) 75°. For the graph a), a continuous line indicates a non-existing region.

Interesting behaviors can be best observed when the data is sorted with respect to energy:

- At higher energies (above 400 eV), we observed a complete removal of the crystalline slab, overrun by the thickness of the amorphous and transitive regions. This is observed in the graphs for the crystalline regions (graphs a and d) in **figure 5**). This is consistent with the observations made above.
- There is a correlation between lower impact energy, increased contaminant implantation and diminishing argon implantation. More specifically, we output a comparison between each region of interest in **figure 6,** showing the slabs between 1.4 and 2.0 Å. The Silicon – Oxygen and Silicon – Hydrogen bond lengths, which are respectively 1.6 Å and 1.46 Å, and, give a peak in this region which can be used to estimate the water implantation. At lower energies, the peak intensities related to water species is at its highest, whereas the argon implantation peak seems to be at its lowest. The behavior is the same at 83° but lost at higher energies. To preserve the readability only RDF results for 75 degrees are displayed, the RDF graphs for the other angles can be found in the supporting information.
- At higher energy above 400 eV, for angles above 60°, the water species related peak intensities coming from Si-O and Si-H interactions are strongly reduced which indicates a significant removal of the contaminant. This translates to an overall increased sputtering yield as will be discussed in a later section.

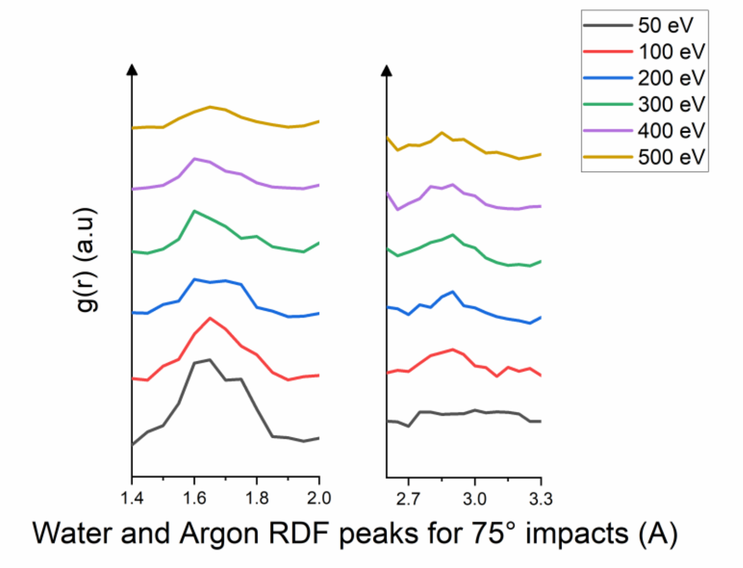

Figure 6: Zoom on the two regions of interest for 75° impacts. On the left, the Si-O and Si-H peaks related to water indicated by bond lengths between 1.4 and 2 Angstrom, and on the right the Si-Ar peak indicating presence of argon in the sample and more precisely in the silicon interstitials which is indicated by a peak between 2.7 and 3.3 Angstrom.

To further confirm the hypothesis that higher energy argon atoms at grazing incidence do not produce amorphization, we will proceed to analyze the implantation depths of the contaminants and argon atoms in the sample.

Implantation depths

The distribution of implanted argon is extremely sensitive to the impact energy and incidence angle, and so is the implantation of the atoms of the water molecules. Their implantation depends on the energy transmitted to the water molecules via elastic collisions with argon atoms or other species in the sample. **Figure 7** shows the evolution of the implantation depth of argon atoms for the different experimental conditions. These graphs show the importance of the incidence angle when low implantation depths are required. With increasing incidence energy, the implantation depth is increasing, as expected. The argon implantation depth is minimized at grazing incidence. For angles above 75°, even at higher energies the simulation results show that almost no argon is implanted into the sample. The same implantation graphs were drawn for oxygen and hydrogen (cf. supporting information). **Figure 8** shows the amount of argon, hydrogen and oxygen implanted in the sample, and **figure 9** the mean implantation depths for the three species. These two figures summarize all the implantation distributions. While we can see in **figure 8** a quasi-linear decrease of the counts of oxygen and hydrogen, we can observe that argon implantation is very sensitive to energy and angle: the implantation is maximum at 500 eV, which was expected, yet we see that the highest angles have a minimal implantation of argon, while retaining the lowest counts for both oxygen and hydrogen for almost all angles. Additionally in **figure 9** that the implantation depth varies linearly with energy, which should be expected since higher energy will induce deeper penetration in the sample. More argon particles are implanted, and their implantation is deeper. On the other hand, this trend is minimized at 83°, while the removal of contaminant is not minimized at these high angles. The last point will be discussed in the section on the sputtering of clusters.

For 50 eV argon ions, there is almost no implantation: the energy of the impacts is barely high enough for argon to penetrate into the sample, and the argon will remain extremely close to the surface. A lot of backscattering is observed. At 500 eV, the argon ions implantation is increased, but towards grazing incidence, implantation remains minimal. This is interesting for milling processes where the sample should stay as pristine as possible. Since there are almost no argon implantations, it is safe to assume that the contaminant will play a major role in the amorphization of the sample. This observation is especially interesting as we can find some conditions where the contaminants are quite efficiently removed. We started to underline this set of conditions in the previous section, and we will pursue the discussion in the forthcoming sections.

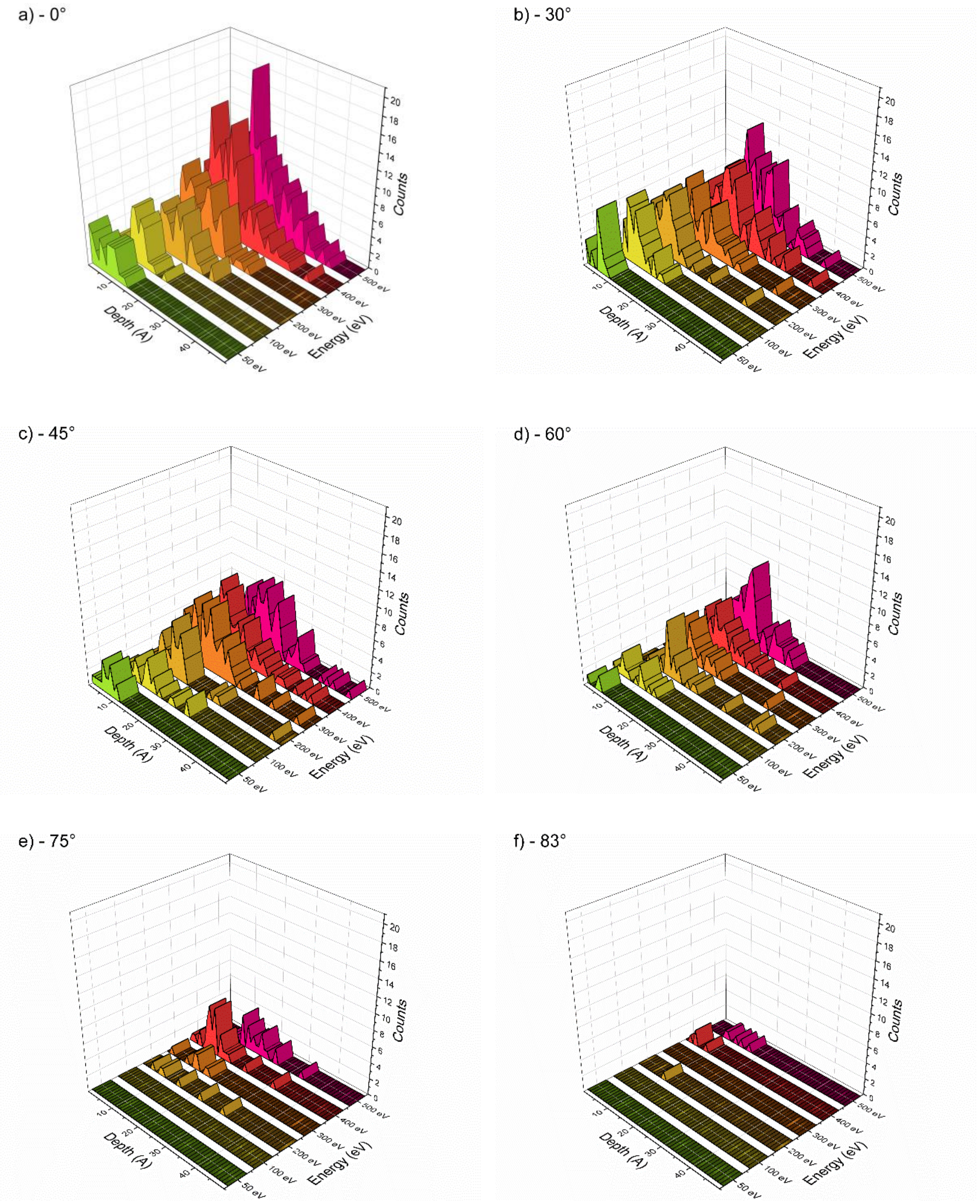

Figure 7: Implantation depth of argon atoms for incidence angles of a) 0°, b) 30°, c) 45°, d) 60°, e) 75° and f) 83°.

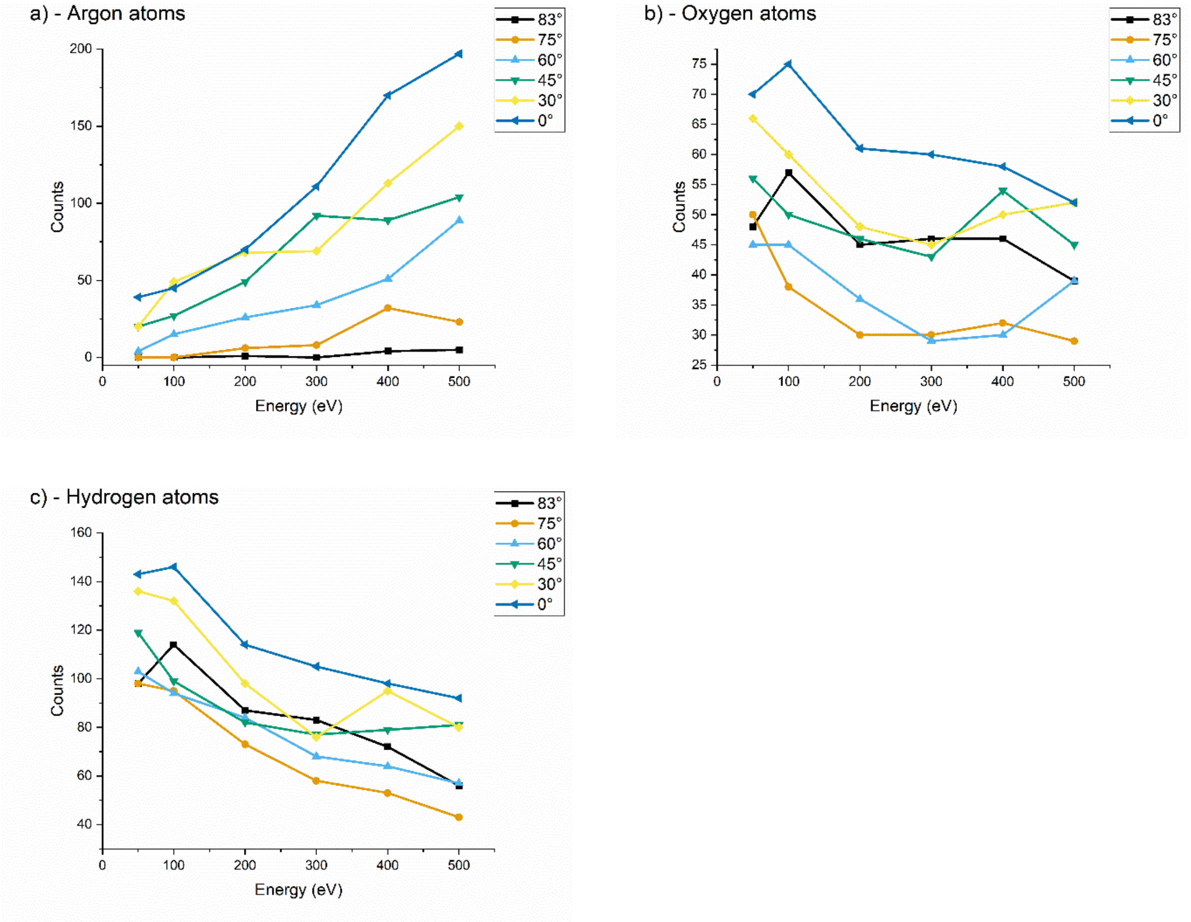

Figure 8: Total implantation counts of a) argon atoms , b) oxygen atoms and c) hydrogen atoms in the sample with respect to the impact energy for the different incidence angles.

In **figures 8 and 9** when observing the graphs related to the contaminants, we can see that the mean implantation depths of the contaminants are rather homogeneous compared to the implantation depths of argon, with a slight difference between oxygen and hydrogen related to their abundance in the water molecule. Due to oxygen’s electronegativity and its strong interaction with silicon, we can assume that free oxygen will tend to pair extremely quickly with silicon, whereas hydrogen can travel deeper into the sample, due to its low mass and via channeling processes. Contaminants tend to remain closer to the surface than argon: the water being deposited at the surface, even higher energy collisions will only transmit a fraction of the energy to the water molecules, which will be either sputtered or fragmented and implanted. Hence, the resulting penetration depth of hydrogen and oxygen should be shallower than for argon. It is interesting to observe that at higher energies, the total number of implanted oxygen and hydrogen atoms is reduced, meaning that a higher energy will favor the removal of contaminants. This behavior is further enhanced at angles above 75°. At 83° and 500 eV, is the most favorable situation for contaminant removal, which also favors sample purity since fewer argon atoms are implanted into the sample. This hypothesis made on the contamination removal will be confirmed in the section on the sputtering yields.

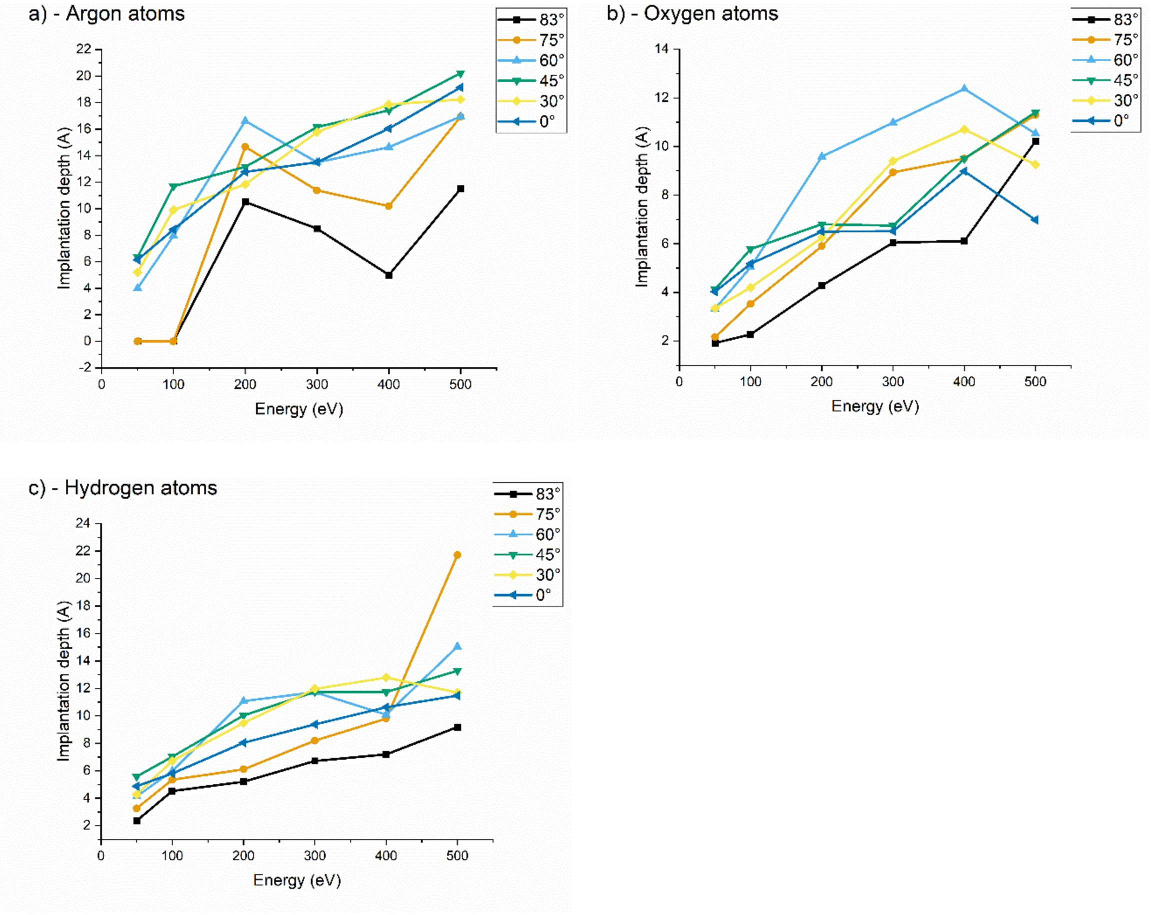

Figure 9: Mean implantation depth of a) argon atoms , b) oxygen atoms and c) hydrogen atoms in the sample with respect to the impact energy for the different incidence angles.

Sputtering yields

The sputtering yield in ion irradiation experiments is especially interesting since it is one of a few parameters that can be measured in experiments. Hence, sputtering yields have been thoroughly studied in the past, yet, at the low impact energies of 500 eV and below they are less well known. Only few studies investigated ultra-low energy argon impacts[38–44], let alone the variation of the sputtering yields with respect to angle variations. Previous studies differ from our in several aspects: Zalm et. al[41]. have extensively studied the energy dependence, but their impact angle remained at normal incidence, and the energy of impact was far greater than the range studied in this publication. Despite these differences, we could compare some of our results in 2 points situated below the 500 eV threshold. In the publication by Timonova et. al[40], the MEAM potential is used to model 500 eV impacts at 45°, which corresponds to a specific case of our study and allowed us to cross-check another data point. In the work of Sycheva et. al[44], the ZBL potential is used to perform 50 – 300 eV impacts at normal incidence, which was similar to our methodology and allowed us to compare our ReaxFF potential results with the different potentials they used. In the investigations described by Lee et. al[42], Ar^+ and O_2^+ ions were used to perform the sputtering, and the publication describes extensively the case for 0, 40 and 70° impacts at 500 eV. Our methodology involved an in-depth analysis of several angles as well as several energies in the extremely low energy range (between 50 and 500 eV). While this methodology is presented here for silicon, there is no doubt it could be applied to other materials. The key aspect, and what makes this publication new in the scope of the previously cited publications is the range of angles and energies that have been studied, as well as the presence of a contamination layer.

In this section we have plotted the sputtering yields for all impact energies and incidence angles to try to understand the mechanisms of sputtering at such low energies (**figure 10).** The silicon sputtering yields follow the expected trend with a maximum yield obtained between incidence angles of 55° and 75°. For an impact energy bellow 100 eV, the sputtering threshold is barely reached which causes the sputtering yield to be minimal. At higher energies, the sputtering yields of our simulations are comparable to the data from literature when identical conditions are available:

- Most of the data points we could compare to were situated at 500 eV, and the sputter yield values we obtained matched the ones described in [39,41,42] We could observe similar trends for the angle dependency, and while the sputtering yield did not exactly match their data points, the differences can be explained by the ReaxFF potential used in our simulations.
- We could compare our data points with the publication of Sycheva et. al [44] since they covered the 50 - 300 eV range for 0° incidence, extensively measuring the depth of the amorphous layer, while also giving us a good comparison with the RDF. Furthermore, we obtained yields of the same order of magnitudes.

In the framework of minimizing the sample modification under ion beam irradiation a higher energy, which increases the sputtering yield and at the same time the damage done to the sample due to increased implantation depths, must be avoided. In the ideal case the sample damage is kept minimal during the milling process. When present, most of the contamination layer should be removed but not implanted. When analyzing the sputtering yields of contaminants, we observe the same trend as for silicon: higher energies increase the yield, and we can still observe some angle dependency, with a maximal yield region between 60 – 75°. A difference we observed occurs above 80°

where the sharp decrease which is observed for silicon particles is not present for the species present in water. In our simulations, the water layer is not renewed between each collision, and therefore the sputtering yields of the water species tend to decrease with increasing fluence. Hence, the sputtering yields of water related species do not follow the same trend than silicon. Yet, in general it is comparable: we can still observe that a higher energy tends to give an increased sputter yields for both oxygen and hydrogen particles. Since higher energies also increase the contaminant removal, the trade-off between the removal of contaminant and the increased amorphization depth, is relevant for experimental setups where the sample has been exposed to air for an extensive period, or for experimental chambers with low vacuum levels where contaminant will deposit onto the sample surface. Furthermore, at 83° we can observe a notable drop in silicon sputtering yields, while maintaining a high sputtering yield for O and H, which makes these conditions favorable for materials removal with presence of contaminations. Combined with the previous observations of implantations and damage formation, we start to see a trend where 500 eV collisions at almost grazing incidence would be suitable to mill silicon samples with argon ions. In the next paragraph we will have a closer look at the sputtered products to get a better understanding of the full sputtering mechanisms.

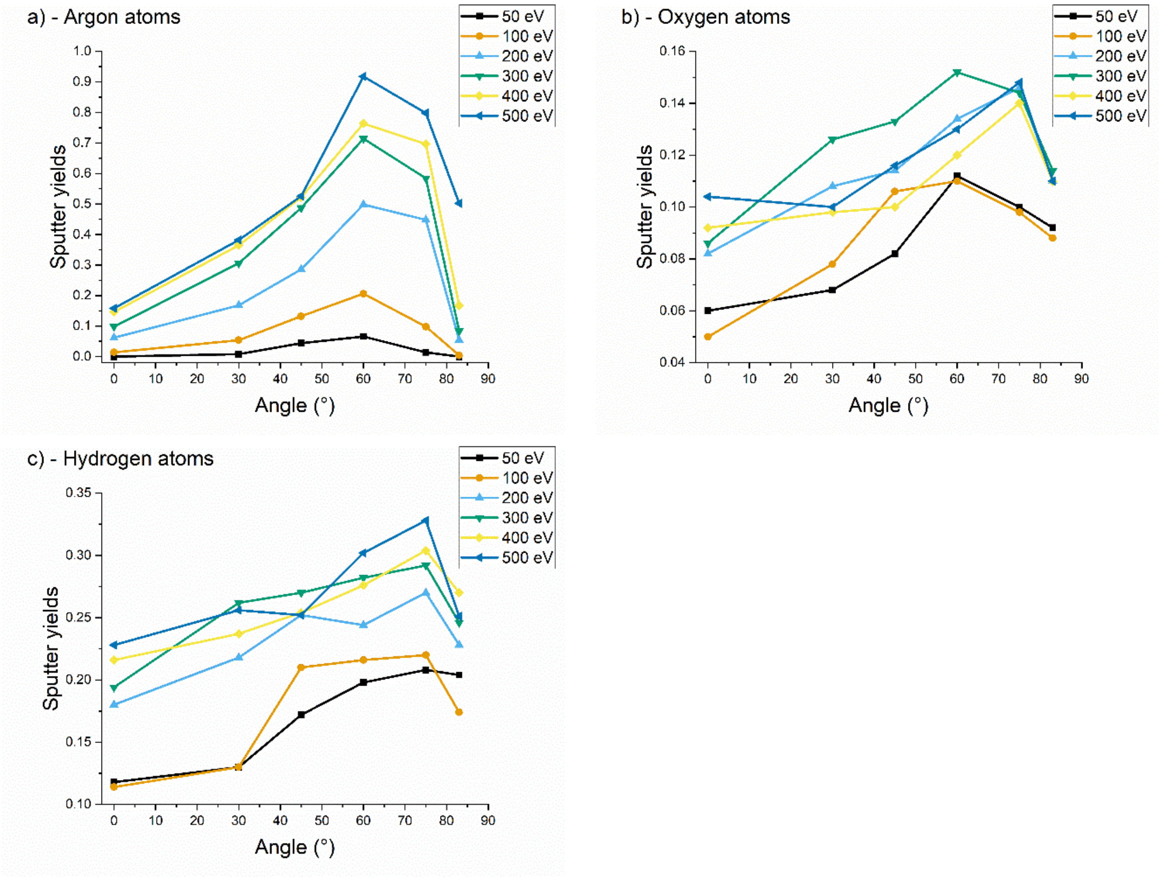

Figure 10: Sputter yields for a) silicon, b) oxygen and c) hydrogen with respect to the angle for each energy.

To measure the impact of the contaminants on the sputtering yields, we sputtered a pristine silicon sample and compared the two series of simulations. Furthermore, we performed Binary Collision Approximation (BCA) simulations on pristine silicon using the SDTrimSP code. In **Figure 11,** the sputtering yields for each of the methods are plotted, as well as a comparison between the three methods used to simulate the sputtering of the silicon sample. On graph c) of **figure 11** we can observe the increasing impact of the contaminant: for low impact energies (50 – 100 eV), the contaminant has a minimal impact on the sputtering yields (> 5%)., However, when increasing the energy we can observe an increased effect of the contaminant on the sputtering yield, leading to lower silicon sputtering yields. This effect is maximal at 500 eV where we can see a difference of approximatively 20%, which can be explained by the fact that for low energy sputtering events (below 100 eV), the low yield variations are so small they can be encompassed in statistical variations, and therefore are less easy to detect than for higher energy sputtering events (300 – 500 eV). At higher energies, we can observe that the contaminant forms a shielding layer on top of the sample which will be preferentially sputtered, as we will see in the next paragraphs.

When looking at the sputtering yields obtained with SDTrimSP, we can observe a very similar trend for MD and SDTrimSP, yet we also observe a significant difference between the yields (figure 12). This can be explained by the difference in the code used. While ReaxFF models bond breaking and forming between atoms, the SDTrimSP – BCA type simulations are used as a reference method for comparison. A general observation between all the methods is the trend, which is kept between each simulation tools, the difference in results being observed in the yield values. Furthermore, SDTrimSP and TRIM use both a fully amorphous target and use purely repulsive interatomic potentials. When comparing closely the trends between ReaxFF, SDTrimSP and TRIM, we observe that the maximum yield is obtained around 60 – 70°, which is identical for the three models.

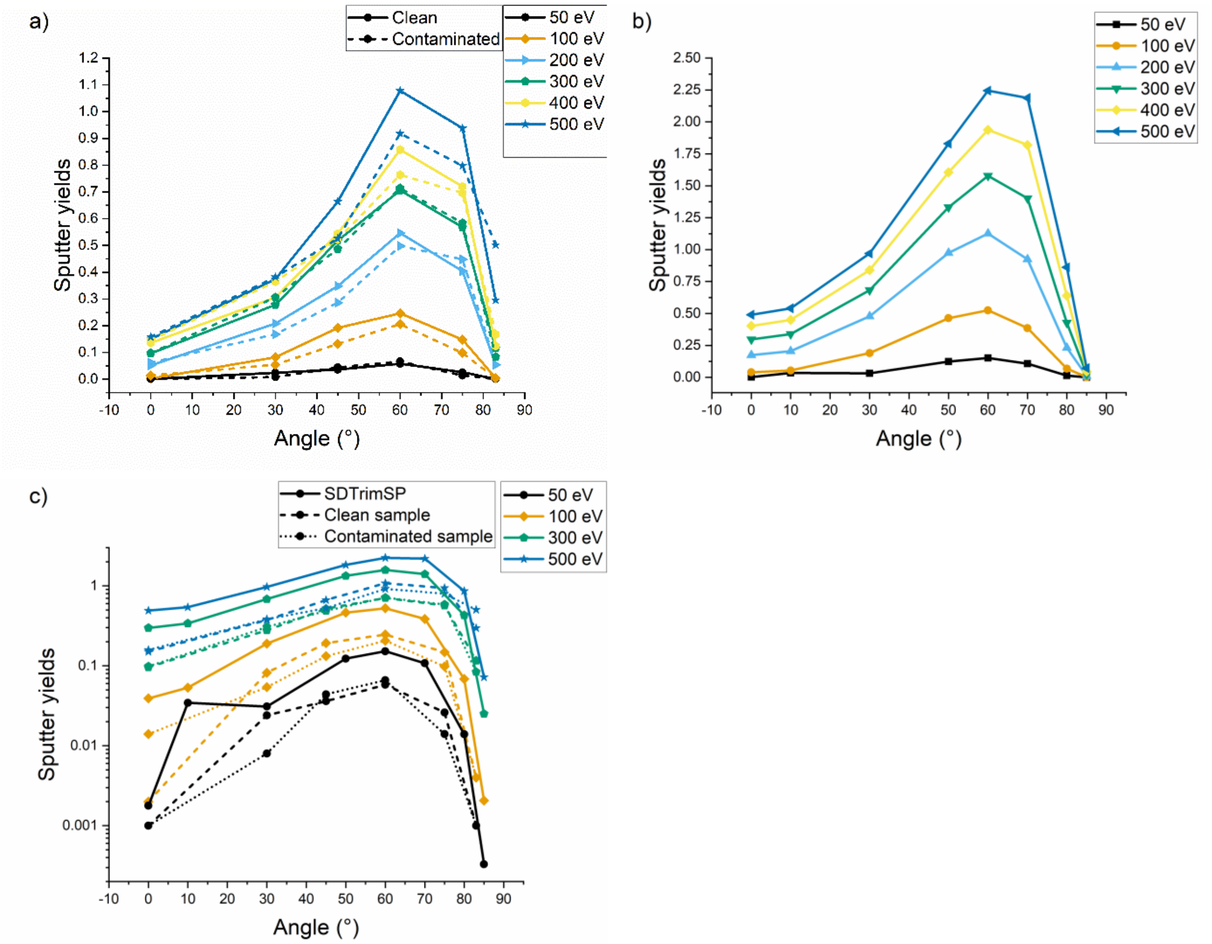

Figure 11: Sputtering yields for a) MD simulationspristine and contaminated silicon sample, b) a clean SDTrimSP simulation of the silicon sample, and c) a logarithmic plot comparing the clean, contaminated and clean SDTrimSP sample.

The sputtering of clusters

For higher impact energies, material can be sputtered in different ways:

- Direct sputtering by elastic collisions [45] from the incident argon. This means the argon collides directly with either a contaminant, a silicon or an argon atom and sputters it.

- Indirect sputtering by elastic chocs from the collision cascade. In this case, the initial collision between the incident argon and a target atom transmits the energy into the lattice, which leads possibly to other displaced atoms in the sample. These displacements can sputter particles when occurring at the sample surface.
- Backscattering of Argon particles. This mechanism usually concerns only argon that is a noble gas and therefore does not form bonds in the sample. This causes argon to be very volatile.

These mechanisms play a role in the final sputtering yields. An interesting outcome of the simulations are the mechanisms leading to the sputtering of clusters. In **figure 12** we plotted the results of the analysis of the sputtered clusters with the highest sputter yields. We included several other partial sputtering yields in the supporting information, such as oxygen – oxygen. A note on the method, Clusters were detected using a threshold on interatomic distance. For silicon clusters, the interatomic threshold we set is inferior to the Si – Si bond length for clustering. Consequently, a direct observation for silicon – silicon clusters in general is that in most cases, silicon atoms are sputtered as Si_2 clusters. The partial Si – Si yield is also a non-negligible fraction of the pure silicon yield (up to 40% for the angles between 60 and 75°). This mechanism is enhanced for increasing impact energies and for larger incidence angles. The second most abundant sputtered clusters are entire water molecules. Since they are deposited on the sample surface, there is at the beginning of the bombardment a high probability to sputter intact water molecules, or to fraction them. Following bombardments can also sputter silicon – oxygen clusters. Due to the strong bond between silicon and oxygen, the silicon – oxygen pair has the same sputtering yield than silicon – hydrogen, despite the fact of hydrogen being twice as abundant in the sample. Finally, very few oxygen – hydrogen, oxygen – oxygen and hydrogen – hydrogen clusters are sputtered (cf. supporting information).

The previously described trends are increased by higher impact energies and larger incidence angles: the sputtering yield of silicon – silicon clusters is enhanced in these conditions similarly to the silicon sputtering yield. We can also observe a similar trend for water related clusters. The trend for water removal is biased by the non-renewal of the water layer, yet we can observe that higher impact energies and incidence angles favor the removal of water molecules, with a maximum at 500 eV and 75°. We can also observe good conditions of water removal in combination with a lower sputtering yield for silicon at 83°. Since the water layer is not renewed in between bombardments, another interesting observation is to measure the probability per collision to fraction a water molecule in order to determine if some water molecules remain intact on the surface after the 500 bombardments.

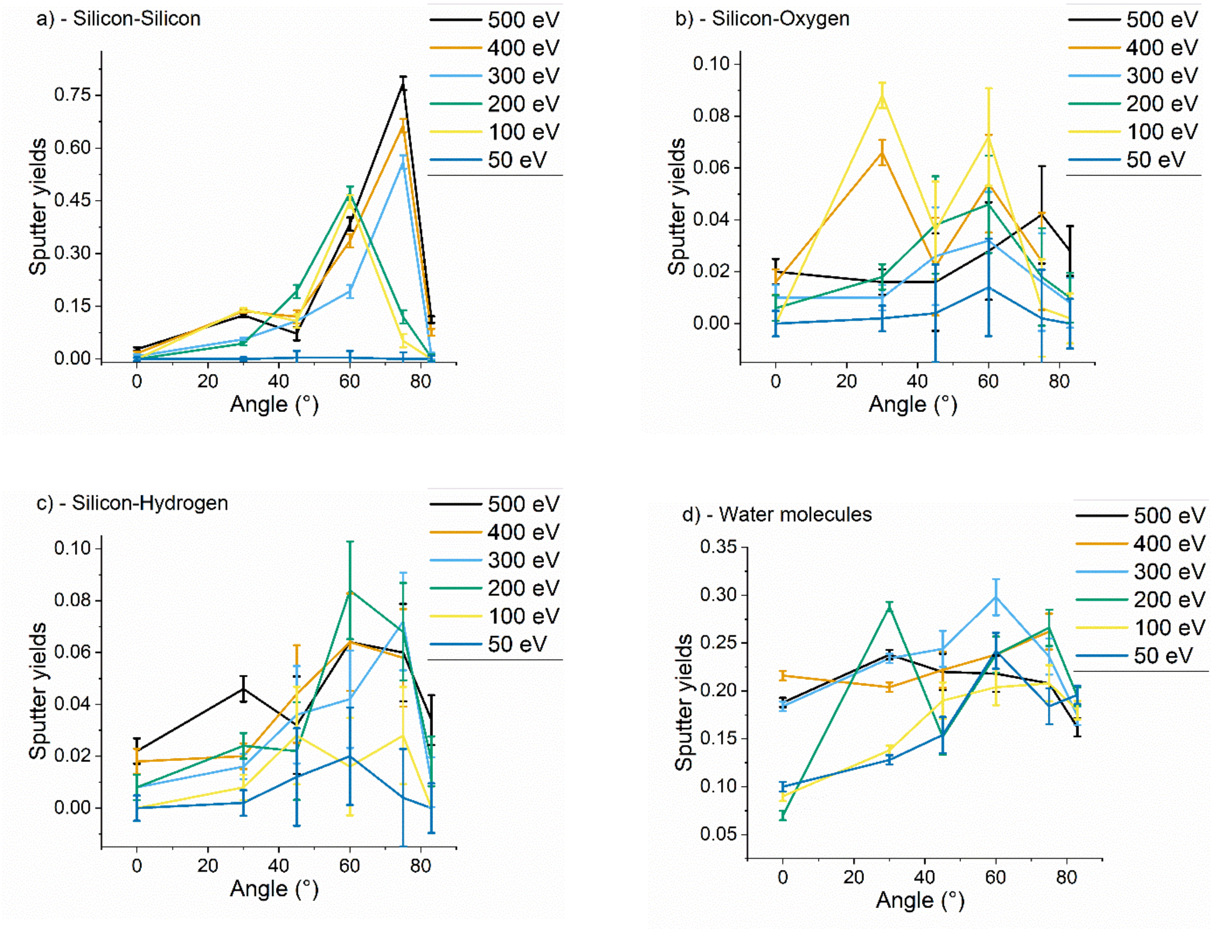

Figure 12: Partial sputter yields of clusters: a) silicon – silicon, b) silicon – oxygen, c) silicon – hydrogen, and d) entire water molecules.

Evolution of the fraction of intact water molecules

The implantation of water species and the amorphization of the sample is strongly correlated to the fragmentation of water molecules during the argon bombardment. Indeed, when water molecules are dissociated, free oxygen atoms or O – H fragments are liberated near the surface, increasing the probability of the formation of a silicon – oxygen bond. Once formed, a silicon – oxygen bond will be notably hard to break and will tend to be sputtered as a whole, as shown in previous section. Thus, water fragmentation plays a key role in the amorphization of the sample, since the bond of Si – O clusters will be i) much stronger than Si – Si or Si – H, and ii) shorter than Si – Si bonds. Therefore, it is easy to understand how the formation of Si – O bonds will modify the local structure, and thus, as shown in previous sections, have an impact on the amorphization coefficient. One of the objectives, i.e. minimizing the impact of the water contamination on the sputtering process, is to remove as much water molecule as possible by sputtering, while minimizing its fragmentation and implantation. In **figure 13** the probability (in percentage) to fragment one water molecule per impact is plotted with respect to the fluence. Since the water layer is not renewed throughout the simulations, at the end of the bombardments the number of intact water molecules tends towards zero. The evolution of the water dissociation probability can be fitted by the $Ae^{(B/x)}$ function. A steep curve indicates fast water fragmentation, while a slowly decreasing curve indicates the presence of intact water particles until high fluences. With increasing bombardment energy, we can observe an increased water fragmentation probability: a higher energy induces bigger collisions cascades, which in return have a higher probability to interact with water molecules and thus have a higher fragmentation probability. Despite this increased probability of fragmentation, we observed that even at a 50 eV impact energy, there are almost no intact water molecules left at the end of the simulations. We also observe that an incidence angle of 60° maximizes the water fragmentation for low impact energies. For high impact energies, the water dissociation probability is highest for large incidence angles. When considering the overall behavior of the water molecules, there is a competition between the water molecule fragmentation and its sputtering. We observed in the sputtering yield section that the intact water molecule yield is maximum at higher incidence angles and impact energies. The probability of fragmentation also increases with respect to the angle and energy. In **figure 14** we plotted the water dissociation probability for 50 and 500 eV collisions, for each angle we selected. From this plot we can deduce a lower chance of water fragmentation at lower energies. At an incidence angle of 83° we observe the lowest probability to fragment water molecules for both 50 and 500 eV. On the other hand at 500 eV, we still have a significant intact water molecules sputtering yield which could indicate an interesting set of parameters for water removal while also retaining a shallow amorphous layer on the sample surface.

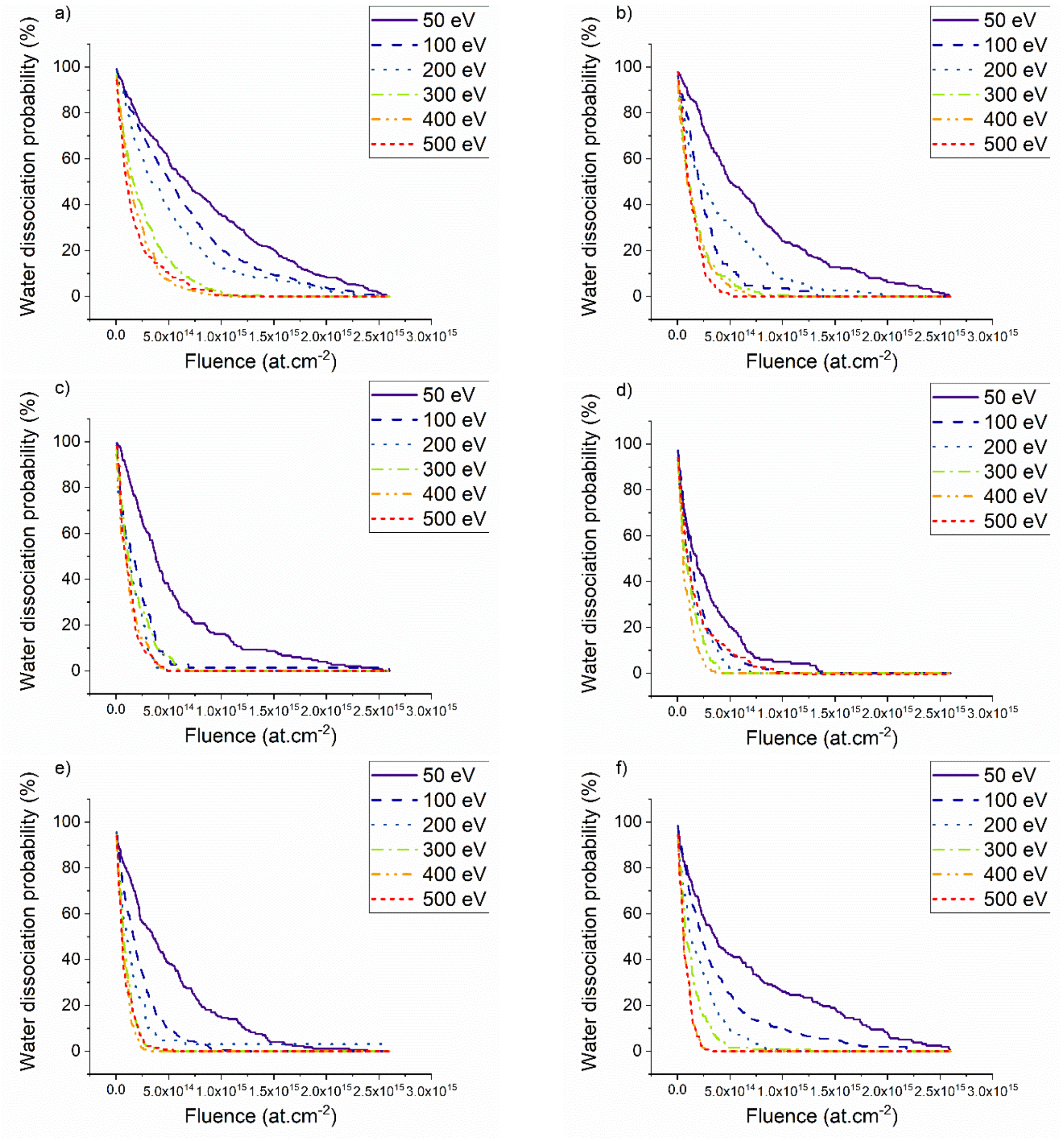

Figure 13: Probability to fragmentation a water molecule per impact with respect to the fluence for each energy at a) 0°, b) 30°, c) 45°, d) 60°, e) 75°, f) 83°

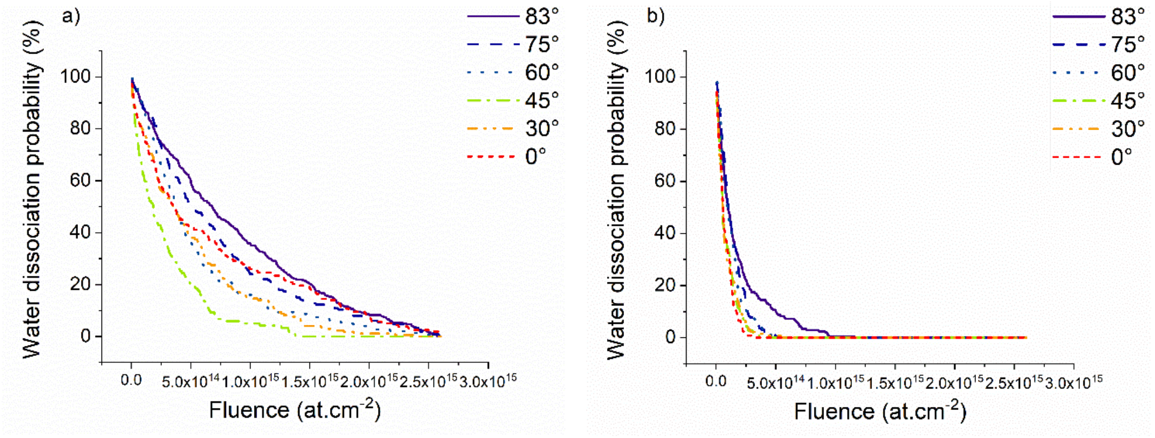

Figure 14: Probability to fragment a water molecule per impact with respect to the fluence for each angle for a) 50 eV impacts and b) 500 eV impacts.

Conclusions

From all the observations made before we can distinguish several interesting cases for the sputtering by ultra-low energy argon ions of silicon covered with a water layer. For applications where the lowest amount of sample damage is required, higher impact energies need to be avoided since the thickness of the amorphous layer increases with energy. The critical role of contaminations on sample amorphization was already observed previously, especially for higher incidence angles since grazing incidence collisions fraction more water molecules, and thus increase the number of contaminant fragments near the surface. For higher impact energies, we show that the sputtering yields of water molecules and fragments is increased, leading to the interesting observation of a competition between i) the amorphization induced by the collisions, by the water fragments and by the implantation of contaminant species, and ii) the reduced implantation of contaminants due to higher sputtering yields.

We observe that grazing incidence collisions can diminish the thickness of the amorphous layer while also maintaining a decent sputtering yields for contaminating particles. More specifically, at 83° incidence, regardless of the energy of impact, we observe that the amorphous layer thickness is significantly reduced compared to other angles. Considering the low number of implanted argon atoms, the low concentration of remaining contaminant species remaining at the end of the sputtering and the decreased sputtering yields (compared to incidence angles in the range of 60 – 80°), it is safe to assume this set of conditions is optimal for the removal of the contaminating layer on top of the sample. These conditions are of interest for applications such as

TEM lamella preparation or milling processes. Moreover, in this condition set, higher energies do not induce a significant increase to the amorphous layer depth: there is a competition between water fragmentation and water sputtering which, at higher angles, leads to a preferential sputtering of the molecules instead of fragmenting the molecules.

Simulations give us access to atomic-scale parameters that cannot be obtained in experiments, and which are interesting for the fundamental understanding of sputtering mechanics. These simulations were performed with only one kind of contaminant, and without renewal of this water layer. Some interesting future simulations could include other type of contaminants, as nitrogen or carbon-containing impurities that are extremely often found in instrument chambers, and the renewal of contamination layer during the sputtering process.

References

(1) MacH, J.; Šamoil, T.; Voborn, S.; Kolíbal, M.; Zlámal, J.; Spousta, J.; Dittrichov, L.; Šikola, T. *Review of Scientific Instruments* **2011**, *82*, 1–8. doi:10.1063/1.3622749

(2) Nebiker, P. W.; Döbeli, M.; Mühle, R.; Suter, M.; Vetterli, D. *Nucl Instrum Methods Phys Res B* **1996**, *113*, 205–208. doi:10.1016/0168-583X(95)01366-0

(3) Moreno-Barrado, A.; Castro, M.; Gago, R.; Vázquez, L.; Muñoz-García, J.; Redondo-Cubero, A.; Galiana, B.; Ballesteros, C.; Cuerno, R. *Phys Rev B Condens Matter Mater Phys* **2015**, *91*, 1–12. doi:10.1103/PhysRevB.91.155303

(4) Hecht, J. D.; Frost, F.; Hirsch, D.; Neumann, H.; Schindler, A.; Preobrajenski, A. B.; Chassé, T. *J Appl Phys* **2001**, *90*, 6066–6069. doi:10.1063/1.1415765

(5) Gotoh, Y.; Kagamimori, K.; Tsuji, H.; Ishikawa, J. *Surf Coat Technol* **2002**, *158–159*, 729–731. doi:10.1016/S0257-8972(02)00262-1

(6) Teichmann, M.; Lorbeer, J.; Ziberi, B.; Frost, F.; Rauschenbach, B. *New J Phys* **2013**, *15*. doi:10.1088/1367-2630/15/10/103029

(7) Gago, R.; Vázquez, L.; Cuerno, R.; Varela, M.; Ballesteros, C.; Albella, J. M. *Nanotechnology* **2002**, *13*, 304–308. doi:10.1088/0957-4484/13/3/313

(8) Fritzsche, M.; Muecklich, A.; Facsko, S. *Appl Phys Lett* **2012**, *100*, 0–4. doi:10.1063/1.4721662

(9) Wei, B. Q.; Zhou, X.; Joshi, B.; Chen, Y.; Li, K. D.; Wei, Q.; Sun, K.; Wang, L. *Advanced Materials* **2009**, *21*, 2865–2869. doi:10.1002/adma.200803258

(10) Ensinger, W. *Nucl Instrum Methods Phys Res B* **1997**, *127–128*, 796–808. doi:10.1016/S0168-583X(97)00010-4

(11) Amano, J.; Bryce, P.; Lawson, R. P. W. *J Vac Sci Technol* **1976**, *13*, 591–595. doi:10.1116/1.569040

(12) Soong, C.; Woo, P.; Hoyle, D. *Micros Today* **2012**, *20*, 44–48. doi:10.1017/s1551929512000752

(13) Zhang, G. P.; Schwaiger, R.; Volkert, C. A.; Kraft, O. *Philos Mag Lett* **2003**, *83*, 477–483. doi:10.1080/0950083031000151383

(14) Rubanov, S.; Munroe, P. R. *Micron* **2004**, *35*, 549–556. doi:10.1016/j.micron.2004.03.004

(15) Giannuzzi, L. A.; Drown, J. L.; Brown, S. R.; Irwin, R. B.; Stevie, F. A. *Microsc Res Tech* **1998**, *41*, 285–290. doi:10.1002/(SICI)1097-0029(19980515)41:4<285::AID-JEMT1>3.0.CO;2-Q

(16) Bender, H.; Franquet, A.; Drijbooms, C.; Parmentier, B.; Clarysse, T.; Vandervorst, W.; Kwakman, L. *Semicond Sci Technol* **2015**, *30*, 114015. doi:10.1088/0268-1242/30/11/114015

(17) Grant, J. T.; Walck, S. D.; Scheltens, F. J.; Voevodin, A. A. *Materials Research Society Symposium - Proceedings* **1997**, *480*, 49–71. doi:10.1557/proc-480-49

(18) Rodenburg, C.; Jepson, M. A. E.; Bosch, E. G. T.; Dapor, M. *Ultramicroscopy* **2010**, *110*, 1185–1191. doi:10.1016/j.ultramic.2010.04.008

(19) Lotnyk, A.; Poppitz, D.; Ross, U.; Gerlach, J. W.; Frost, F.; Bernütz, S.; Thelander, E.; Rauschenbach, B. *Microelectronics Reliability* **2015**, *55*, 2119–2125. doi:10.1016/j.microrel.2015.07.005

(20) Mehrtens, T.; Bley, S.; Venkata Satyam, P.; Rosenauer, A. *Micron* **2012**, *43*, 902–909. doi:10.1016/j.micron.2012.03.008

(21) Prokhodtseva, A.; Mulders, J.; Vystavel, T. *Microscopy and Microanalysis* **2017**, *23*, 298–299. doi:10.1017/s1431927617002173

(22) Roediger, P.; Wanzenboeck, H. D.; Hochleitner, G.; Bertagnolli, E. *Journal of Vacuum Science & Technology B: Microelectronics and Nanometer Structures* **2009**, *27*, 2711. doi:10.1116/1.3244628

(23) Abdel-Samad, S.; Abdel-Bary, M.; Kilian, K. *Vacuum* **2005**, *78*, 83–89. doi:10.1016/j.vacuum.2005.01.001

(24) Ren, Y.; Lei, D.; Yao, F.; Wang, Z. *AIP Conf Proc* **2019**, *2126*. doi:10.1063/1.5117635

(25) Pal, G.; Yadav, R. C.; Akhter, J.; Das, T.; Sarkar, A.; Mallik, C.; Bhandari, R. K. *J Phys Conf Ser* **2012**, *390*, 1–6. doi:10.1088/1742-6596/390/1/012045

(26) Defoort-Levkov, G. R. N.; Bahm, A.; Philipp, P. *Beilstein Journal of Nanotechnology* **2022**, *13*, 986–1003. doi:10.3762/bjnano.13.86

(27) Fogarty, J. C.; Aktulga, H. M.; Grama, A. Y.; Van Duin, A. C. T.; Pandit, S. A. *Journal of Chemical Physics* **2010**, *132*. doi:10.1063/1.3407433

(28) Newsome, D. A.; Sengupta, D.; Foroutan, H.; Russo, M. F.; Van Duin, A. C. T. *Journal of Physical Chemistry C* **2012**, *116*, 16111–16121. doi:10.1021/jp306391p

(29) Thompson, A. P.; Aktulga, H. M.; Berger, R.; Bolintineanu, D. S.; Brown, W. M.; Crozier, P. S.; in 't Veld, P. J.; Kohlmeyer, A.; Moore, S. G.; Nguyen, T. D.; Shan, R.; Stevens, M. J.; Tranchida, J.; Trott, C.; Plimpton, S. J. *Comput Phys Commun* **2022**, *271*, 108171. doi:10.1016/j.cpc.2021.108171

(30) Costa Filho, R. N.; Alencar, G.; Skagerstam, B. S.; Andrade, J. S. *EPL* **2013**, *101*. doi:10.1209/0295-5075/101/10009

(31) Aktulga, H. M.; Fogarty, J. C.; Pandit, S. A.; Grama, A. Y. *Parallel Comput* **2012**, *38*, 245–259. doi:10.1016/j.parco.2011.08.005

(32) Cowen, B. J.; El-Genk, M. S. *Comput Mater Sci* **2016**, *111*, 269–276. doi:10.1016/j.commatsci.2015.09.042

(33) Huang, L.; Kieffer, J. *Journal of Chemical Physics* **2003**, *118*, 1487–1498. doi:10.1063/1.1529684

(34) Kulkarni, A. D.; Truhlar, D. G.; Goverapet Srinivasan, S.; Van Duin, A. C. T.; Norman, P.; Schwartzentruber, T. E. *Journal of Physical Chemistry C* **2013**, *117*, 258–269. doi:10.1021/jp3086649

(35) Rappe, A. K.; Goddard III, W. A. *Journal of Physical Chemistry* **1991**, *95*, 3358–3363

(36) Aiichiro, N. *Comput Phys Commun* **1997**, *104*, 59–69

(37) Kopera, B. A. F.; Retsch, M. *Anal Chem* **2018**, *90*, 13909–13914. doi:10.1021/acs.analchem.8b03157

(38) Hofsäss, H.; Stegmaier, A. *Nucl Instrum Methods Phys Res B* **2022**, *517*, 49–62. doi:10.1016/j.nimb.2022.02.012

(39) Sycheva, A. A.; Voronina, E. N.; Rakhimova, T. V. *Journal of Surface Investigation* **2018**, *12*, 1270–1277. doi:10.1134/S1027451019010191

(40) Timonova, M.; Lee, B. J.; Thijsse, B. J. *Nucl Instrum Methods Phys Res B* **2007**, *255*, 195–201. doi:10.1016/j.nimb.2006.11.023

(41) Zalm, P. C. *J Appl Phys* **1983**, *54*, 2660–2666. doi:10.1063/1.332340

(42) Lee, H. I.; Moon, D. W.; Shin, H. C.; Oh, S. K.; Kang, H. J. The Surface Transient Effect in the Si Sputtering Yield by Low Energy O2+ and Ar+ Ion Bombardments. In *Nuclear Instruments and Methods in Physics Research, Section B: Beam Interactions with Materials and Atoms*; 2004; Vol. 219–220, pp 959–962. doi:10.1016/j.nimb.2004.01.196

(43) Shumilov, A. S.; Amirov, I. I. *Journal of Surface Investigation* **2020**, *14*, 935–943. doi:10.1134/S1027451020050195

(44) Sycheva, A. A.; Voronina, E. N.; Palov, A. P. *Journal of Surface Investigation* **2019**, *13*, 1272–1279. doi:10.1134/S1027451019060521

(45) Smith, D. P. *Surf Sci* **1971**, *25*, 171–191. doi:10.1016/0039-6028(71)90214-7

Supporting Information

Supporting information summary:

Publication supplements

Figure S1 Evolution of the amorphization coefficient for a specific case comparing 50 and 500 eV for each angle.

Figure S2 Evolution of the thickness of the crystalline slab with respect to the energy of impact and the angle

Figure S3 Implantation depth charts for each angle and energy for oxygen atoms, full display of the distributions.

Figure S4 Implantation depth charts for each angle and energy for hydrogen atoms, full display of the distributions.

Figure S5 Partial sputter yields for clusters with minimal sputter yields (O – O, H – H and O – H)

ReaxFF Potential

ReaxFF Potential: The force field parameters from the supporting information of J. Phys. Chem. C 2012, 116, 16111–16121 were also used in this study.

Acknowledgements

We want to acknowledge the Luxembourg National Research Fund (FNR) for their contribution in the form of financial support thanks to the grant C17/MS/11682850/ULOWBEAM. We want to acknowledge and thank Dr. Chad Rue, Dr. Richard J. Young from Thermo Fisher Scientific and Dr. Tom Wirtz from

Luxembourg Institute of Science and Technology for their comments and suggestions, as well as for their interesting observations in the redaction of this manuscript.

Funding

This project was supported by the National Research Fund (FNR), Luxembourg (C17/MS/11682850/ULOWBEAM).